PHYSICAL REVIEW MATERIALS **4**, 054415 (2020)

Editors' Suggestion

In situ TEM observation of nanodomain mechanics in barium titanate under external loads

Takashi Sumigawa,[*] Ken Hikasa,[†] Akihisa Kusunose, Hiroki Unno, Kairi Masuda, Takahiro Shimada,
and Takayuki Kitamura

Department of Mechanical Engineering and Science, Kyoto University, Nishikyo-ku, Kyoto 615-8540, Japan

(Received 16 December 2019; revised manuscript received 24 March 2020; accepted 20 April 2020;
published 19 May 2020)

In ferroelectrics, domain walls have significant effects on ferroic properties. The mechanical behavior of domain walls has been investigated because of its scientific and technological importance. Numerous experiments and simulations have examined domain walls and their motion under mechanical strain. However, since nano- and micromechanical testing is challenging, previous studies have mainly involved indirect or intermittent observations, and there have been few real-time *in situ* observations. As a result, the mechanism by which mechanical loads induce wall motion remains elusive. Here, we directly observe stress-induced domain wall motion in real time by using rationally designed specimens and transmission electron microscopy (TEM). We imaged the domain walls directly as they moved and disappeared depending on the mechanical conditions during the experiments. Furthermore, we experimentally determined the mechanical criteria for wall motion. Our results not only provide fundamental knowledge about ferroelectrics but also provide information on how to control their dynamics from an engineering standpoint.

DOI: 10.1103/PhysRevMaterials.4.054415

I. INTRODUCTION

Domain walls in ferroelectrics have attracted significant attention in the field of materials science. Although the walls compose a nanoscale substructure [1,2], they have significant effects on ferroic properties such as piezoelectricity and dielectric properties [3,4]. The study of domain walls has so far been mainly geared towards enhancing ferroic properties. Nanodomain engineering to form highly concentrated domain walls is a promising route to achieving extraordinary device performance [5–7]. Recently, in addition to these common properties, the discovery of new functionalities associated with domain walls, such as conductivity [8,9], multiferroic properties [10], and photovoltaic effects, has focused more and more attention on ferroelectrics [11]. Utilizing domain walls will be essential for next-generation nanoscale devices.

In this context, the mechanical behavior of domain walls under varying mechanical stimulation or loading is a critical issue. Domain walls are displaced easily by external mechanical stress, and a number of stress-induced wall motions have been suggested in the literature. For example, the stress-strain curve for $BaTiO_3$ under compression exhibits plastic-deformation-like behavior at low stress levels, which can be explained by wall motion [12,13]. Furthermore, piezoresponse force microscopy has shown displacement of walls following loading [14,15], and “mechanical writing” actively utilizes this electromechanical coupling to control nanodomains [16]. In addition to experiments, a number of simulations such as *ab initio*, molecular dynamics (MD), and phase-field simulations have demonstrated wall motion under various stress conditions [17–20]. However, despite its importance, direct, or real-time, *in situ* observation of stress-induced wall motion has rarely been reported, owing to the difficulty of controlled nano- and micromechanical testing [21–24]. Thus, even domain wall motion under tensile loads has not been fully clarified.

Moreover, the mechanical behavior of a domain wall cannot be completely understood under homogeneous mechanical stress. It has been reported that under spatially inhomogeneous mechanical conditions, the walls become curved [25] by, for example, bowing [26]. Characterizing such behavior is both scientifically and technologically important since ferroelectrics are starting to be utilized in flexible devices [27]. However, to our knowledge, there has so far not been any real-time observation of a curved wall structure and its evolution under controlled inhomogeneous mechanical conditions. Through bending, we can subject a domain wall to inhomogeneous mechanical stress with both tensile and compressive components. The gradient of the stress, that is, inhomogeneity, can be controlled by the degree of bending. Thus, the development of wall motion under inhomogeneous mechanical conditions can be investigated by bending, although this is challenging at the nanoscale.

Here, by fabricating rationally designed shapes from $BaTiO_3$, we have been able to control tensile and bending conditions at the nanoscale and directly observe 90° domain wall motion by transmission electron microscopy (TEM). Moreover, by capturing the very moment when a wall begins to move in real time, we can identify the mechanical criterion. Not only do our results provide fundamental knowledge about ferroelectrics, but they also contribute to nanoengineering

---

[*] sumigawa@cyber.kues.kyoto-u.ac.jp

[†] hikasa.ken.34r@st.kyoto-u.ac.jp

2475-9953/2020/4(5)/054415(8)

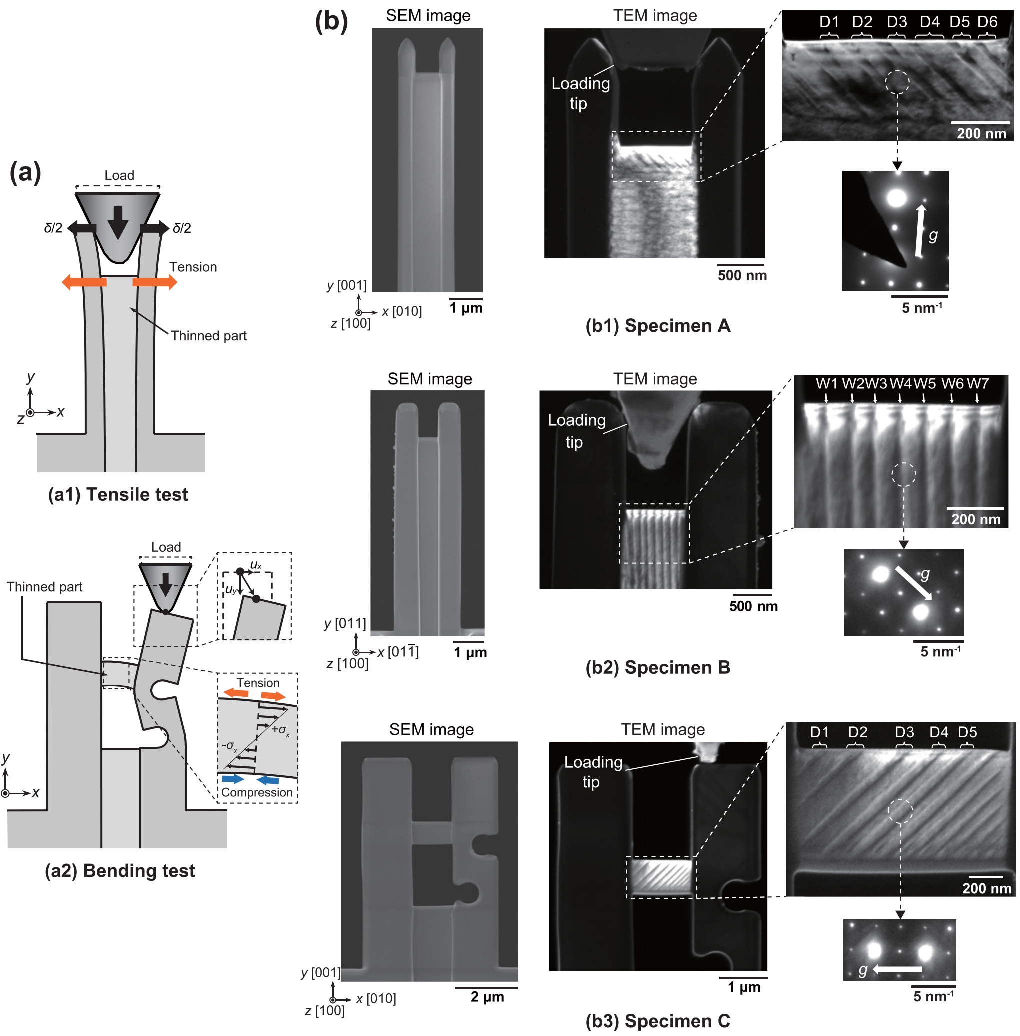

FIG. 1. (a) Schematics of the designed tensile and bending tests. (a1) Tensile test: opening displacement δ is applied by inserting the tip, and the thinned part undergoes tension. (a2) Bending test: on pushing the tip, the loading point is displaced by u_x and u_y, and the thinned part undergoes bending. (b) SEM and TEM dark-field images of specimens A, B, and C after fabrication and annealing. The diffraction patterns indicate the selected diffraction spots.

applications that require wall motion control, i.e., wall-based nanodevices.

II. RESULTS AND DISCUSSION

Figure 1(a) shows schematics of the tensile and bending tests conducted using a double-cantilever beam with a thinned central part [28]. By inserting a truncated square-pyramid-type indenter between the two beams, an opening displacement δ is applied, and the thinned sections undergo a tensile load, as shown in Fig. 1(a1). In the bending test, the bottom part of the thinned section is cut out, and two notches are introduced in the beams. By pushing the top of the beam, the loading point is displaced by $(u_x, -u_y)$ from its original position, and bending is applied to the thinned part [Fig. 1(a2)]. Figure 1(b) shows scanning electron microscopy (SEM) and dark-field TEM images of specimens A, B, and C, fabricated from BaTiO$_3$ using a focused ion beam (see Supplemental Material S1 [29]). Here, specimens A and B are specimens for tensile testing, and the crystal orientation of specimen B is rotated by 45° with respect to specimen A. Specimen C is for the bending test without a rotation of crystal orientation. The nanostripes seen at the top of specimens A, B, and C are thought to represent 90° domains [30–33]. There are split spots in the diffraction patterns (Fig. S1.3.1), whose splitting direction is diagonal to the diffraction lattice. This corroborates our conclusion that we are seeing 90° domains, based on the TEM study of BaTiO$_3$ by Hu *et al.* [34]. We label each domain in specimens A and C and each domain wall in specimen B, as shown in Figs. 1(b1)–1(b3).

Figure 2(a) shows dark-field TEM images of specimen A during loading (Supplemental Material S2 and Movie 1 [29]) and schematics where the domain outlines are determined by visual inspection. The double beam is gradually opened, and the walls of domain D4 begin to move. We define the beginning of motion as the time at which the wall is displaced by about 5 nm from its original position. Following the motion of domain D4, other walls begin to move as well [Fig. 2(a2)]. Finite-element method (FEM) analysis with an opening displacement δ shows that the thinned part

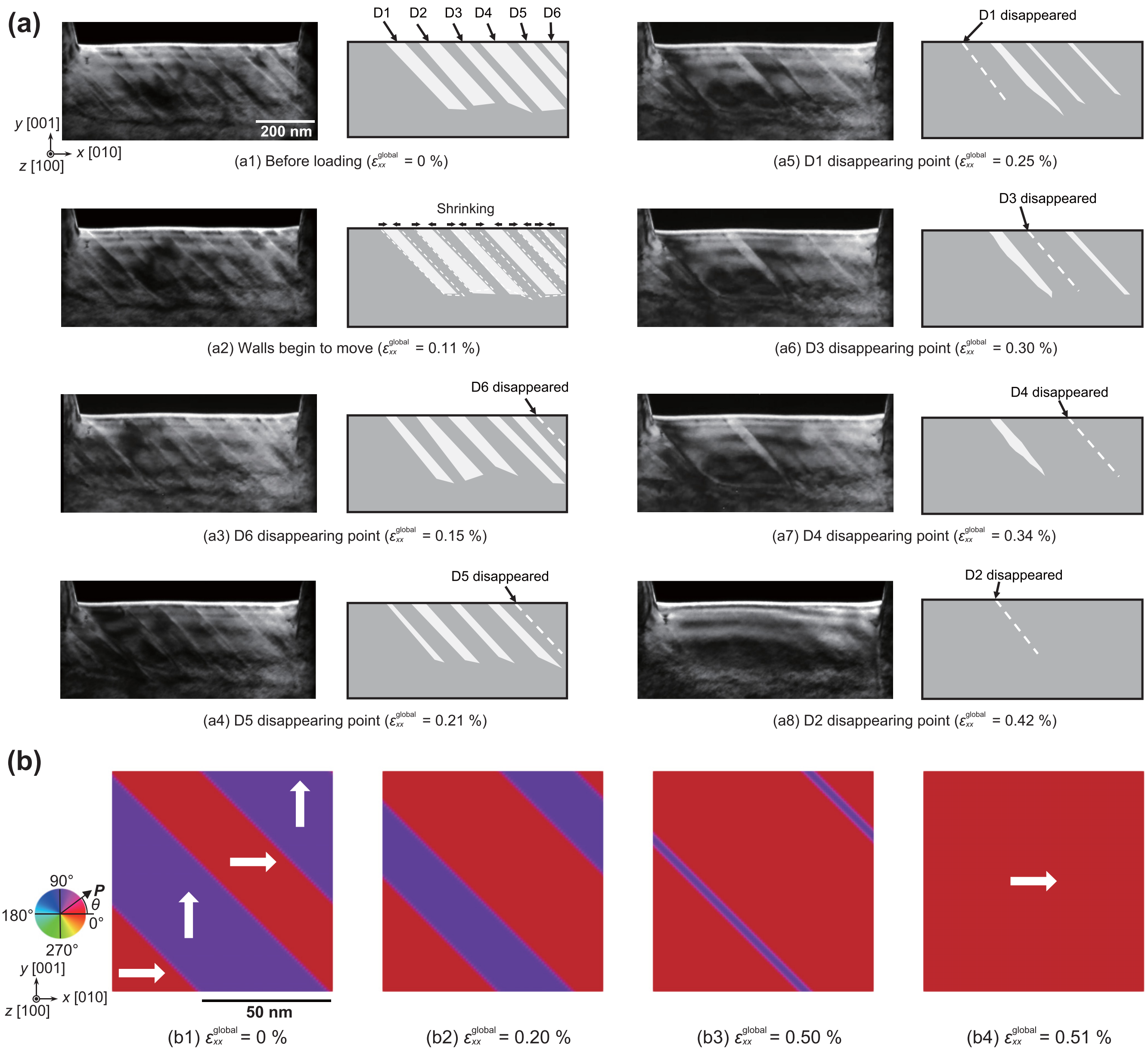

(a1) Before loading ($\varepsilon_{xx}^{\mathrm{global}}$ = 0 %)

(a5) D1 disappearing point ($\varepsilon_{xx}^{\mathrm{global}}$ = 0.25 %)

(a2) Walls begin to move ($\varepsilon_{xx}^{\mathrm{global}}$ = 0.11 %)

(a6) D3 disappearing point ($\varepsilon_{xx}^{\mathrm{global}}$ = 0.30 %)

(a3) D6 disappearing point ($\varepsilon_{xx}^{\mathrm{global}}$ = 0.15 %)

(a7) D4 disappearing point ($\varepsilon_{xx}^{\mathrm{global}}$ = 0.34 %)

(a4) D5 disappearing point ($\varepsilon_{xx}^{\mathrm{global}}$ = 0.21 %)

(a8) D2 disappearing point ($\varepsilon_{xx}^{\mathrm{global}}$ = 0.42 %)

(b1) $\varepsilon_{xx}^{\mathrm{global}}$ = 0 %

(b2) $\varepsilon_{xx}^{\mathrm{global}}$ = 0.20 %

(b3) $\varepsilon_{xx}^{\mathrm{global}}$ = 0.50 %

(b4) $\varepsilon_{xx}^{\mathrm{global}}$ = 0.51 %

FIG. 2. (a) TEM dark-field images and schematics of specimen A under loading. We calculate the global strain $\epsilon_{xx}^{\mathrm{global}}$ the thinned part undergoes by dividing the change in length at the top of the thinned part by the initial length. (b) Phase-field modeling and calculation of domain motion under tension. Contour color and arrow indicate the direction of polarization $\boldsymbol{P}$.

is under x directional tensile strain (Supplemental Material S3 [29]). Table I lists the local strain and stress that each domain wall undergoes when it begins to move. We obtain $\epsilon_{xx}^{\mathrm{local}} = 0.10\% \pm 0.03\%$ and $\sigma_{xx}^{\mathrm{local}} = 111 \pm 34$ MPa, respectively. With increasing load, domain D6 disappears in a snapping manner [Fig. 2(a3)]. Then, D5, D1, D3, D4, and D2 disappear one by one [Figs. 2(a4), 2(a5), 2(a6), 2(a7), and 2(a8)]. As a result, a single domain covers the entire thinned area of the specimen. To elucidate the above behavior, we performed phase-field simulations (Supplemental Material S4 [29]) [35]. Figure 2(b) shows the domain behavior under a tensile strain lateral to the domains. With increasing strain, the domain walls gradually move, which corresponds to the behavior of specimen A. Finally, the total polarization points in the same direction, and the domain structures disappear. This simulation proves that the behavior of specimen A represents stress-induced domain wall motion.

Specimen B exhibits a completely different behavior (Fig. 3(a) and Supplemental Material, Movie 2 [29]). Even under tensile strain, its domain walls do not move, and the width of the domains does not change. The domain wall W7 disappears abruptly at an applied strain of 0.25% [Fig. 3(a2)], followed by the disappearances of W1, W3, W6, W5, W4, and W2, in that order, with increasing tensile strain [Figs. 3(a3), 3(a4), 3(a5), 3(a6), 3(a7), and 3(a8)], and the domain structure disappears completely in the thinned part of the specimen. This process differs entirely from the behavior of specimen A under tensile loading, even though the tested area is covered by a single domain. Figure 3(b) shows the domain behavior

TABLE I. Mechanical conditions to which each domain wall in specimen A is subjected when it begins to move: local strain $\epsilon_{xx}^{\mathrm{local}}$, local stress $\sigma_{xx}^{\mathrm{local}}$, and shear stress parallel to the walls τ_{wall} at the upper part of specimen A.

Wall	$\epsilon_{xx}^{\mathrm{local}}$ (%)	$\sigma_{xx}^{\mathrm{local}}$ (MPa)	τ_{wall} (MPa)
D1			
Left	0.12	126	−63
Right	0.13	144	−72
D2			
Left	0.09	97	−49
Right	0.11	114	−57
D3			
Left	0.07	79	−40
Right	0.08	87	−44
D4			
Left	0.07	77	−39
Right	0.07	77	−39
D5			
Left	0.08	86	−43
Right	0.07	79	−39
D6			
Left	0.10	110	−55
Right	0.09	94	−47

under a tensile strain perpendicular to the domains obtained by the phase-field simulation. The walls in the stripe domain do not move under the external tensile load. However, with increasing strain, the angle of polarization changes drastically in the whole domain [Fig. 3(b4)], and explicit domain structures disappear without wall movement, as in the case of specimen B. These simulations indicate that the behavior of specimen B is rather like a phase transition from the tetragonal to orthorhombic crystal structure.

In specimen C, we observe wall motion that differs from that in specimens A and B (Fig. 4(a) and Supplemental Material, Movie 3 [29]). With increased loading, domains D1, D2, and D3 begin to expand at the top of the specimen, while the domains at the bottom shrink and disappear [Figs. 4(a2) and 4(a3)]. Table II lists the local strain and stress for each domain wall in specimen C, obtained by the FEM at the moment when the wall begins to move. The critical strain and stress for walls D1–D3 are $\epsilon_{xx}^{\mathrm{local}} = 0.09\% \pm 0.03\%$ and $\sigma_{xx}^{\mathrm{local}} = 99 \pm 34$ MPa, respectively. In the bottom parts of walls D4 and D5, which are under compression, the critical strain and stress are $\epsilon_{xx}^{\mathrm{local}} = -0.19\% \pm 0.03\%$ and $\sigma_{xx}^{\mathrm{local}} = -207 \pm 28$ MPa, respectively. With increasing load, D1 and D2 disappear by connecting with each other, while D3 becomes separated in the middle of the specimen [Fig. 4(a3)]. In the final state [Fig. 4(a4)], no explicit domain wall is observed, and we can no longer detect the domain configuration. The FEM shows that through bending, we achieved inhomogeneous mechanical conditions comprising both tension and compression. When the level of inhomogeneity, which corresponds to the stress gradient in this case, is small, a domain wall responds to it by forming a curvature. However, when the inhomogeneity increases, the wall breaks, probably because the curvature becomes too sharp to sustain. Thus, domain walls behave differently depending on the inhomogeneity. As shown by the above results for homogeneous tension, the stress intensity is the parameter that dominates wall motion. However, bending observations clearly reveal that wall motion is also governed by the level of inhomogeneity.

Figure 4(b) shows the phase-field simulation for domains under bending, where the p_x domain is a domain with polarization pointing in the x direction and the p_y domain is a domain with polarization pointing in the y direction. With increasing strain, p_x domains expand at the top, while p_y domains expand at the bottom [red and green regions in Fig. 4(b2)]. Then, other p_y domains appear at the bottom [purple regions in Fig. 4(b3)]. As a result, p_x domains are dominant at the top, while p_y domains are dominant at the bottom [Fig. 4(b4)]. Since the expanding and shrinking processes in the present experiment are similar, we conclude that when the applied stress is low [Fig. 4(a2)], p_x domains expand at the top, while p_y domains expand at the bottom. However, when inhomogeneity increases, we cannot determine the domain state owing to the absence of explicit domain walls. Nevertheless, we believe that because of the stress distribution, the p_x domains at the top will coexist with the p_y domains at the bottom. By contrast, in the central area under bending, there is a transition region from tension to compression where the stress is small. In this region, domains are likely to behave in a complex manner, leading to, for example, the nucleation of a new domain, as suggested by the phase-field simulation [purple regions in Fig. 4(b3)]. As a result, under a high applied stress, the final domain state may not be as simple as merely the coexistence of p_x and p_y domains. This remains to be investigated in a future study.

The present study is the first to apply tension and bending to domain walls in a controlled, systematic fashion and provide images of stress-induced domain wall motion in real time. Our results provide fundamental knowledge about ferroelectrics, and the present method, i.e., the use of TEM and specially designed specimens, can be applied to other areas of research, such as room-temperature stress-induced ferroelectricity in $\mathrm{SrTiO_3}$ [36–38] and flexoelectricity [39–41], whereas the phase-field simulation results coincide well with experimental results. This indicates that, although they are based on empirical parameters, multiscale methods such as phase-field simulations are a powerful tool to predict ferroelectric properties, which is difficult for *ab initio* simulations owing to the huge computational cost.

In order to find the mechanical criterion for wall motion, we focus on the shear stress parallel to the wall τ_{wall}, described as

$$\tau_{\mathrm{wall}} = -\frac{\sigma_{xx} - \sigma_{yy}}{2} \sin 2\theta + \tau_{xy} \cos 2\theta, \tag{1}$$

where σ_{xx}, σ_{yy}, and τ_{xy} are stress components. θ is the angle between the domain wall and the y axis. τ_{wall} is zero in specimen B because the wall and the loading directions are perpendicular ($\theta = 90°$), while τ_{wall} is not zero in specimen A ($\theta = 45°$), as shown in Figs. 5(a) and 5(b). In specimen C, τ_{wall} is opposite at the top and bottom, and domain walls propagate in opposite directions [Fig. 5(c)]. Thus, τ_{wall} corresponds to the observed wall motions.

The domain walls do not begin to move until the stress reaches a certain value. The critical shear stress is estimated to

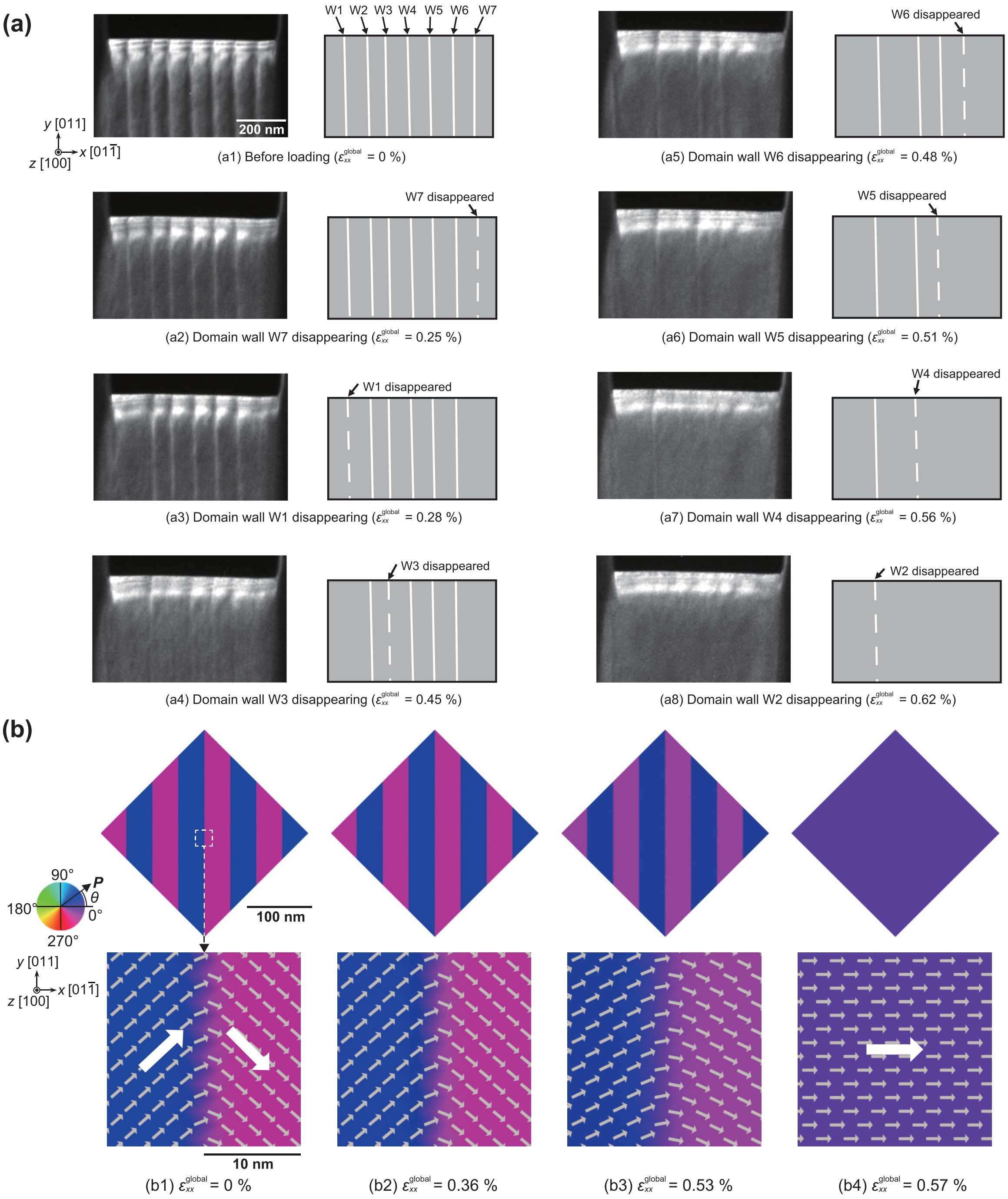

(b1) $\varepsilon_{xx}^{\text{global}}$ = 0 % (b2) $\varepsilon_{xx}^{\text{global}}$ = 0.36 % (b3) $\varepsilon_{xx}^{\text{global}}$ = 0.53 % (b4) $\varepsilon_{xx}^{\text{global}}$ = 0.57 %

FIG. 3. (a) TEM dark-field images and schematics of specimen B under loading. (b) Phase-field modeling and calculation of domain motion under tension perpendicular to the wall.

be 56 ± 17 MPa based on specimen A. This is comparable to the value of 50 ± 17 MPa obtained for D1–D3 for specimen C and the stress amplitude necessary for indentation-induced domain switching (61 MPa) for 0.65PMN-0.35PT [42]. On the other hand, for D4 and D5 in specimen C, we obtain 104 ± 14 MPa as the critical stress, which differs significantly from the above value. This may be attributable to the influence of stress normal to the wall. Density functional theory simulations of domain walls in $PbTiO_3$ [17] suggest that domain wall motion is actually a change in covalent bonding, i.e., the breaking and reconstruction of bonds (Pb-O bonds, in that particular study), and that the critical stress is equivalent to the stress necessary for breaking those bonds. The interatomic distance expands under tensile conditions and shrinks under compressive conditions. Therefore, covalent bonds are more likely to break under tension than under compression, which leads to a difference in critical stress [43]. Moreover, the domain walls in our experiments may interact with each other.

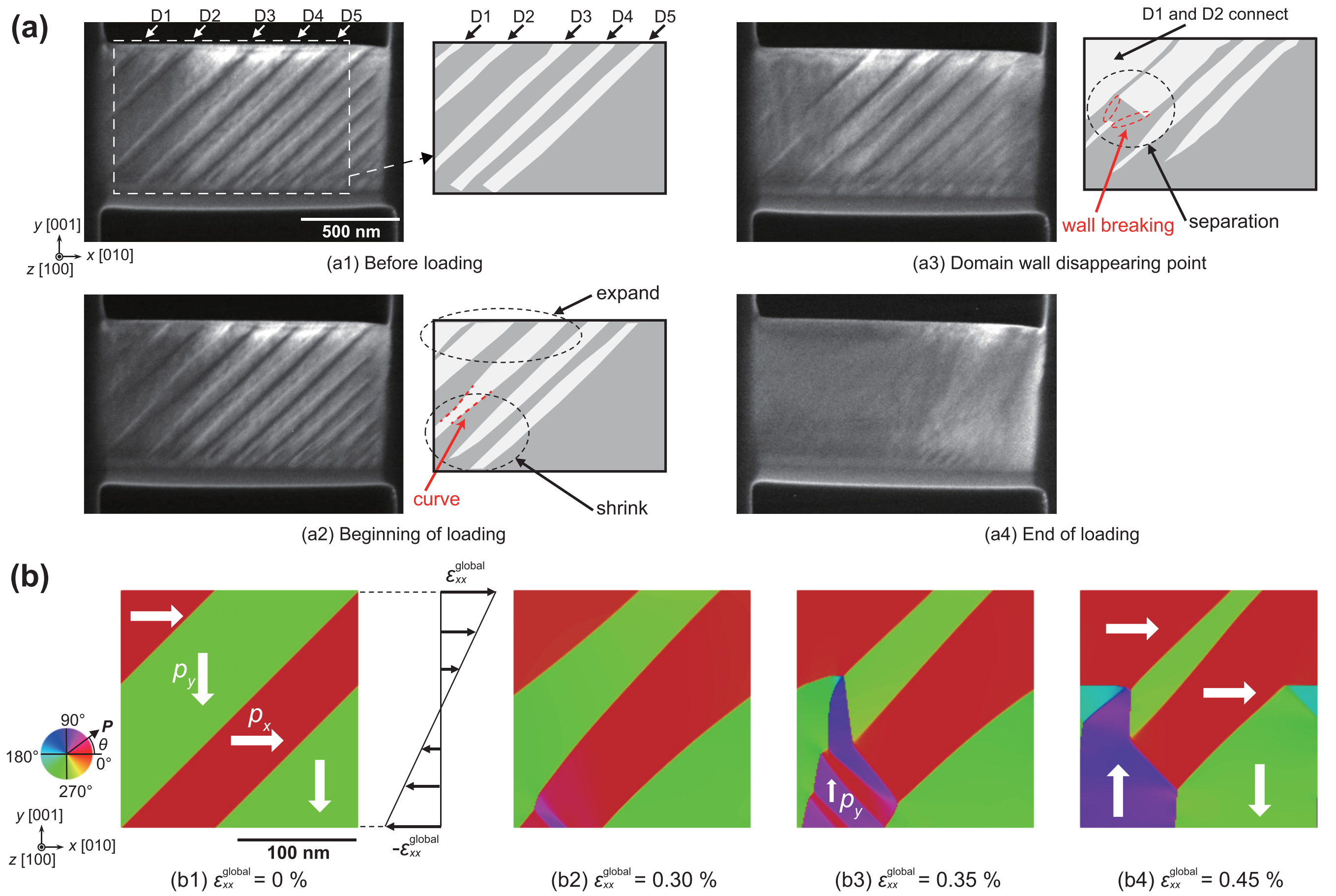

FIG. 4. (a) TEM dark-field images and schematics of specimen C under loading. (b) Phase-field modeling and calculation of domain motion induced by a bending strain, i.e., tension at the top and compression at the bottom.

In $BaTiO_3$, when the distance between the two walls is about 3 μm, a compressive stress of 6 MPa is needed to initiate wall motion [15], which is much lower than the value we obtained in the present study. According to Kubo and Umeno, MD simulations of $PbTiO_3$ suggest that the electric field induced by a domain wall may cause long-range interaction and affect wall behavior [18]. Therefore, the critical stress obtained may also be affected by neighboring walls. This remains to be investigated in future studies.

TABLE II. Mechanical conditions for each domain wall in specimen C when the wall begins to move.

Wall	ϵ_{xx}^{local} (%)	σ_{xx}^{local} (MPa)	τ_{wall} (MPa)
D1			
Left	0.11	120	−60
Right	0.10	111	−55
D2			
Left	0.12	132	−66
Right	0.10	110	−55
D3			
Left	0.09	98	−49
Right	0.06	66	−33
D4			
Left	−0.21	−235	118
Right	−0.20	−223	111
D5			
Left	−0.18	−201	100
Right	−0.16	−179	90

Finally, in regards to the significance of the mechanical criterion, although the value we obtained remains approximate at this stage, it can be used as a starting point for designing or engineering domain-wall-based electronic devices because undesired wall motions can degrade device performance. A good example of such a device is domain wall memory, which utilizes the conductivity of walls [44]. When mechanical vibrations from the environment or other components exceed the mechanical criterion, the domain walls also vibrate, and the electric currents may decrease or disappear because they are disturbed by the wall motions. Therefore, engineers must design devices on the basis of this important mechanical threshold.

III. CONCLUSION

We developed specially designed specimens to conduct nanoscale tensile and bending tests on $BaTiO_3$ in a TEM instrument and thus observed stress-induced domain wall motion in real time. Domain walls may or may not move under tensile stress and propagate in different directions under bending stress. We found that this motion is driven by shear

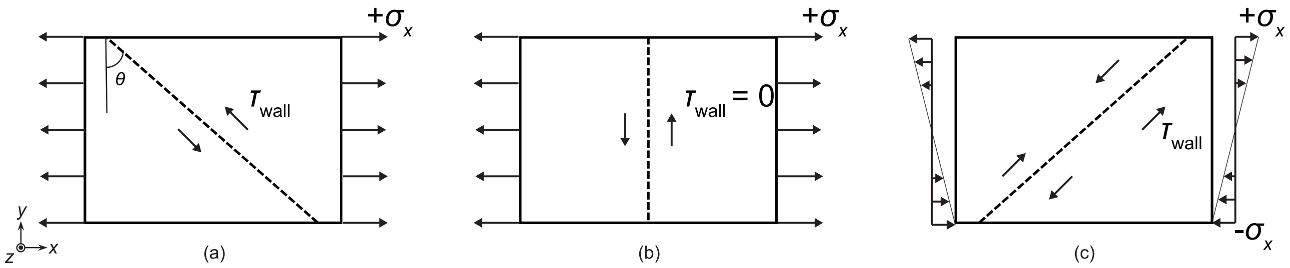

FIG. 5. Schematics of shear stress parallel to domain walls τ_{wall} induced by loading. (a)–(c) Specimens A, B, and C, respectively. The dotted line indicates the wall. θ is the angle between the wall and the y axis.

stresses parallel to the domain wall. The critical values were determined to be 56 ± 17 MPa under tensile conditions and 104 ± 14 MPa under compressive conditions.

ACKNOWLEDGMENT

This work was supported by JSPS KAKENHI Grants No. JP18H05241, No. JP18H03753, and No. JP18K18807.

---

[1] W. J. Merz, Domain formation and domain wall motions in ferroelectric BaTiO$_3$ single crystals, Phys. Rev. **95**, 690 (1954).

[2] C.-L. Jia, S.-B. Mi, K. Urban, I. Vrejoiu, M. Alexe, and D. Hesse, Atomic-scale study of electric dipoles near charged and uncharged domain walls in ferroelectric films, Nat. Mater. **7**, 57 (2008).

[3] N. Bassiri-Gharb, I. Fujii, E. Hong, S. Trolier-McKinstry, D. V. Taylor, and D. Damjanovic, Domain wall contributions to the properties of piezoelectric thin films, J. Electroceramics **19**, 49 (2007).

[4] E. A. Little, Dynamic behavior of domain walls in barium titanate, Phys. Rev. **98**, 978 (1955).

[5] G. Catalan, J. Seidel, R. Ramesh, and J. F. Scott, Domain wall nanoelectronics, Rev. Mod. Phys. **84**, 119 (2012).

[6] V. Nagarajan, A. Roytburd, A. Stanishevsky, S. Prasertchoung, T. Zhao, L. Chen, J. Melngailis, O. Auciello, and R. Ramesh, Dynamics of ferroelastic domains in ferroelectric thin films, Nat. Mater. **2**, 43 (2003).

[7] S. Wada, K. Muraoka, H. Kakemoto, T. Tsurumi, and H. Kumagai, Enhanced piezoelectric properties of potassium niobate single crystals by domain engineering, Jpn. J. Appl. Phys. **43**, 6692 (2004).

[8] J. Seidel, L. W. Martin, Q. He, Q. Zhan, Y.-H. Chu, A. Rother, M. E. Hawkridge, P. Maksymovych, P. Yu, M. Gajek, N. Balke, S. V. Kalinin, S. Gemming, F. Wang, G. Catalan, J. F. Scott, N. A. Spaldin, J. Orenstein, and R. Ramesh, Conduction at domain walls in oxide multiferroics, Nat. Mater. **8**, 229 (2009).

[9] J. Guyonnet, I. Gaponenko, S. Gariglio, and P. Paruch, Conduction at domain walls in insulating Pb(Zr$_{0.2}$ Ti$_{0.8}$)O$_3$ thin films, Adv. Mater. **23**, 5377 (2011).

[10] T. Xu, T. Shimada, Y. Araki, J. Wang, and T. Kitamura, Multiferroic domain walls in ferroelectric PbTiO$_3$ with oxygen deficiency, Nano Lett. **16**, 454 (2016).

[11] S. Y. Yang, J. Seidel, S. J. Byrnes, P. Shafer, C.-H. Yang, M. D. Rossell, P. Yu, Y.-H. Chu, J. F. Scott, J. W. Ager, L. W. Martin, and R. Ramesh, Above-bandgap voltages from ferroelectric photovoltaic devices, Nat. Nanotechnol. **5**, 143 (2010).

[12] M. N. Shetty, V. C. S. Prasad, and E. C. Subbarao, 90° domain-wall motion in barium titanate under uniaxial compression, Phys. Rev. B **10**, 4801 (1974).

[13] V. C. S. Prasad and E. C. Subbarao, Deformation studies on BaTiO$_3$ single crystals, Appl. Phys. Lett. **22**, 424 (1973).

[14] K. Kim and J. E. Huber, *In Situ* observation of ferroelastic domain evolution in a near-morphotropic Pb(Zr, Ti)O$_3$ ceramic by piezoresponse force microscopy, J. Eur. Ceram. Soc. **35**, 1459 (2015).

[15] J. Muñoz-Saldaña, G. A. Schneider, and L. M. Eng, Stress induced movement of ferroelastic domain walls in BaTiO$_3$ single crystals evaluated by scanning force microscopy, Surf. Sci. **480**, L402 (2001).

[16] H. Lu, C.-W. Bark, D. E. de los Ojos, J. Alcala, C. B. Eom, G. Catalan, and A. Gruverman, Mechanical writing of ferroelectric polarization, Science **336**, 59 (2012).

[17] T. Shimada, Y. Umeno, and T. Kitamura, *Ab initio* study of stress-induced domain switching in PbTiO$_3$, Phys. Rev. B **77**, 094105 (2008).

[18] A. Kubo and Y. Umeno, Atomistic model calculation of stress-induced domain wall instability in PbTiO$_3$ using shell model, J. Solid Mech. Mater. Eng. **6**, 90 (2012).

[19] A. K. Soh, Y. C. Song, and Y. Ni, Phase field simulations of hysteresis and butterfly loops in ferroelectrics subjected to electro-mechanical coupled loading, J. Am. Ceram. Soc. **89**, 652 (2006).

[20] H. Lu, S. Liu, Z. Ye, S. Yasui, H. Funakubo, A. M. Rappe, and A. Gruverman, Asymmetry in mechanical polarization switching, Appl. Phys. Lett. **110**, 222903 (2017).

[21] Z. Chen, L. Hong, F. Wang, S. P. Ringer, L.-Q. Chen, H. Luo, and X. Liao, Facilitation of Ferroelectric Switching via Mechanical Manipulation of Hierarchical Nanoscale Domain Structures, Phys. Rev. Lett. **118**, 017601 (2017).

[22] Z. Chen, Q. Huang, F. Wang, S. P. Ringer, H. Luo, and X. Liao, Stress-induced reversible and irreversible ferroelectric domain switching, Appl. Phys. Lett. **112**, 152901 (2018).

[23] Z. Chen, L. Hong, F. Wang, X. An, X. Wang, S. Ringer, L.-Q. Chen, H. Luo, and X. Liao, Kinetics of Domain Switching by Mechanical and Electrical Stimulation in Relaxor-Based Ferroelectrics, Phys. Rev. Appl. **8**, 064005 (2017).

[24] P. Gao, J. Britson, C. T. Nelson, J. R. Jokisaari, C. Duan, M. Trassin, S.-H. Baek, H. Guo, L. Li, Y. Wang, Y.-H. Chu, A. M. Minor, C.-B. Eom, R. Ramesh, L.-Q. Chen, and X. Pan,

Ferroelastic domain switching dynamics under electrical and mechanical excitations, Nat. Commun. **5**, 3801 (2014).

[25] T. J. Yang, V. Gopalan, P. J. Swart, and U. Mohideen, Direct Observation of Pinning and Bowing of a Single Ferroelectric Domain Wall, Phys. Rev. Lett. **82**, 4106 (1999).

[26] A. Kontsos and C. M. Landis, Computational modeling of domain wall interactions with dislocations in ferroelectric crystals, Int. J. Solids Struct. **46**, 1491 (2009).

[27] W. Gao, Y. Zhu, Y. Wang, G. Yuan, and J.-M. Liu, A review of flexible perovskite oxide ferroelectric films and their application, J. Materiomics **6**, 1 (2020).

[28] T. Sumigawa, T. Shimada, S. Tanaka, H. Unno, N. Ozaki, S. Ashida, and T. Kitamura, Griffith criterion for nanoscale stress singularity in brittle silicon, ACS Nano **11**, 6271 (2017).

[29] See Supplemental Material at http://link.aps.org/supplemental/10.1103/PhysRevMaterials.4.054415 for methods of sample preparation, *in situ* TEM experiments, finite-element and phase-field simulations, and three visualizations regarding domain wall behavior. The visualizations Specimen A.mpg, Specimen B.mpg, and Specimen C.mpg show domain wall motions obtained by direct TEM observations of specimens A, B, and C under mechanical loads, respectively.

[30] A. Schilling, R. M. Bowman, G. Catalan, J. F. Scott, and J. M. Gregg, Morphological control of polar orientation in single-crystal ferroelectric nanowires, Nano Lett. **7**, 3787 (2007).

[31] A. Schilling, D. Byrne, G. Catalan, K. G. Webber, Y. A. Genenko, G. S. Wu, J. F. Scott, and J. M. Gregg, Domains in ferroelectric nanodots, Nano Lett. **9**, 3359 (2009).

[32] A. L. Roytburd, S. P. Alpay, L. A. Bendersky, V. Nagarajan, and R. Ramesh, Three-domain architecture of stress-free epitaxial ferroelectric films, J. Appl. Phys. **89**, 553 (2000).

[33] Y. Sato, T. Hirayama, and Y. Ikuhara, Real-Time Direct Observations of Polarization Reversal in a Piezoelectric Crystal: $Pb(Mg_{1/3}Nb_{2/3})O_3$-$PbTiO_3$ Studied via In Situ Electrical Biasing Transmission Electron Microscopy, Phys. Rev. Lett. **107**, 187601 (2011).

[34] Y. H. Hu, H. M. Chan, Z. X. Wen, and M. P. Harmer, Scanning electron microscopy and transmission electron microscopy study of ferroelectric domains in doped $BaTiO_3$, J. Am. Ceram. Soc. **69**, 594 (1986).

[35] Y. L. Li and L. Q. Chen, Temperature-strain phase diagram for $BaTiO_3$ thin films, Appl. Phys. Lett. **88**, 072905 (2006).

[36] G. Sheng, Y. L. Li, J. X. Zhang, S. Choudhury, Q. X. Jia, V. Gopalan, D. G. Schlom, Z. K. Liu, and L. Q. Chen, Phase transitions and domain stabilities in biaxially strained (001) $SrTiO_3$ epitaxial thin films, J. Appl. Phys. **108**, 084113 (2010).

[37] J. H. Haeni, P. Irvin, W. Chang, R. Uecker, P. Reiche, Y. L. Li, S. Choudhury, W. Tian, M. E. Hawley, B. Craigo, A. K. Tagantsev, X. Q. Pan, S. K. Streiffer, L. Q. Chen, S. W. Kirchoefer, J. Levy, and D. G. Schlom, Room-temperature ferroelectricity in strained $SrTiO_3$, Nature (London) **430**, 758 (2004).

[38] A. Vasudevarao, A. Kumar, L. Tian, J. H. Haeni, Y. L. Li, C.-J. Eklund, Q. X. Jia, R. Uecker, P. Reiche, K. M. Rabe, L. Q. Chen, D. G. Schlom, and V. Gopalan, Multiferroic Domain Dynamics in Strained Strontium Titanate, Phys. Rev. Lett. **97**, 257602 (2006).

[39] P. Zubko, G. Catalan, A. Buckley, P. R. L. Welche, and J. F. Scott, Strain-Gradient-Induced Polarization in $SrTiO_3$ Single Crystals, Phys. Rev. Lett. **99**, 167601 (2007).

[40] W. Ma and L. E. Cross, Flexoelectric polarization of barium strontium titanate in the paraelectric state, Appl. Phys. Lett. **81**, 3440 (2002).

[41] T. D. Nguyen, S. Mao, Y.-W. Yeh, P. K. Purohit, and M. C. McAlpine, Nanoscale flexoelectricity, Adv. Mater. **25**, 946 (2013).

[42] J. K. Shang and X. Tan, Indentation-induced domain switching in $Pb(Mg_{1/3}Nb_{2/3})O_3$-$PbTiO_3$ crystal, Acta Mater. **49**, 2993 (2001).

[43] J. Pokluda, M. Černý, M. Šob, and Y. Umeno, *Ab initio* calculations of mechanical properties: Methods and applications, Prog. Mater. Sci. **73**, 127 (2015).

[44] P. Sharma, Q. Zhang, D. Sando, C. H. Lei, Y. Liu, J. Li, V. Nagarajan, and J. Seidel, Nonvolatile ferroelectric domain wall memory, Sci. Adv. **3**, e1700512 (2017).